

# Classical vs Quantum Annealing and Manifold Reduction in Soft-Spin Minimizers of Ising Hamiltonians

James S. Cummins<sup>1</sup>, Hayder Salman<sup>2,3</sup> and Natalia G. Berloff<sup>1,\*</sup>

<sup>1</sup>*Department of Applied Mathematics and Theoretical Physics,  
University of Cambridge, Wilberforce Road, Cambridge CB3 0WA, United Kingdom*

<sup>2</sup>*School of Mathematics, University of East Anglia,  
Norwich Research Park, Norwich, NR4 7TJ, UK,*

<sup>3</sup>*Centre for Photonics and Quantum Science, University of East Anglia,  
Norwich Research Park, Norwich, NR4 7TJ, UK*

We investigate the minimization of the Ising Hamiltonians, comparing the dynamics of semi-classical soft-spin models with quantum annealing. We systematically analyze how the energy landscape for the circulant couplings of a Möbius graph evolves with increased annealing parameters. Our findings indicate that these semi-classical models face challenges due to a widening dimensionality landscape. To counteract this issue, we introduce the ‘manifold reduction’ method, which restricts the soft-spin amplitudes to a defined phase space region. Concurrently, quantum annealing demonstrates a natural capability to navigate the Ising Hamiltonian’s energy landscape due to its operation within the comprehensive Hilbert space. Our study indicates that physics-inspired or physics-enhanced optimizers will likely benefit from a blend of classical and quantum annealing techniques.

Pursuing enhanced computing speed and power efficiency has led to exploring alternatives to traditional electronic systems in solving complex tasks. Optical Neural Networks (ONNs) promise unprecedented parallelism, potentially superior speeds, and reduced power consumption. ONNs encode neural weights as phase shifts or changes in light intensity, with activation functions instantiated via nonlinear optical materials or components or via a strong hybridization to matter excitations [1]. They offer the potential to operate in the terahertz range, vastly surpassing the gigahertz frequencies of conventional electronic systems that can be exploited in machine learning and combinatorial optimization. The common feature of ONNs is to utilize a network of optical oscillators dynamically described by a coupled system of soft-spin models on complex-valued field  $\psi_i = r_i \exp[i\theta_i]$  that has the amplitude  $r_i$  (referred to as ‘soft mode’) and phase  $\theta_i$  (discrete e.g.  $\theta_i = \{0, \pi\}$  or continuous ‘spin’) degrees of freedom.

Optical parametric oscillator (OPOs) based coherent Ising machines (CIM) [2–5], lasers [6–8], spatial light modulators [9], lattices of polariton [10, 11], and photon condensates [12], Microsoft analogue iterative machine [13] and Toshiba simulated bifurcation machine [14] can all minimize the classical hard-spin Ising Hamiltonians (HSIH)  $H_I = -\sum_{i,j} J_{ij} s_i s_j$  with  $s_i = \pm 1$  for a coupling matrix  $\mathbf{J}$  and other spin Hamiltonians (e.g. XY Hamiltonians  $H_{XY} = -\sum_{i,j} J_{ij} \mathbf{s}_i \cdot \mathbf{s}_j$  with  $s_i = (\cos \theta_i, \sin \theta_i)$ ) using soft-spin bifurcation dynamics via the Aharonov-Hopf bifurcation [15]. Such soft-spin models exploit enhanced dimensionality, marked by small energy barriers during amplitude bifurcation, but also complicate the energy landscape with numerous local minima. Dimensionality annealing was proposed to bring advantages to physical optimizers by bridging minima separated by sig-

nificant energy barriers [16]. In parallel to these methods, quantum annealing is another approach to minimize the HSIH. Despite numerous studies contrasting classical and quantum methods, the limitations of currently available hardware and limitations of simulating quantum systems classically has led to conflicting conclusions as to whether a quantum advantage can potentially be realized using quantum annealing [17–23] and in particular, how quantum annealers such as D-wave perform in comparison with CIM [24]. In the latter, the connectivity of the coupling matrix was assumed to be a key factor in performance differences between these machines [24].

Here, we analyse and contrast the annealing of semi-classical soft-spin Ising models (SSIM) with quantum annealing for circulant coupling matrices which allow complete control of frustration, energy gaps, and the structure of critical points. A highlighted challenge for SSIM annealing lies in the opposing relationship between local and global minima when mapping the Ising Hamiltonian to the energy of the soft-spin system [25]. Notably, we demonstrate that quantum annealing within the whole Hilbert space of the hard-spin system navigates this challenge. Additionally, we suggest that ‘manifold reduction’, aligning amplitudes to the mean, is needed to augment the likelihood of SSIM annealing finding the global minima.

The ONNs based on laser operation are non-Hermitian systems that tend to minimise losses on their route to coherence. The losses can be written as an ‘energy’ (‘cost’) function to be minimized. For instance, CIM’s energy landscape to be minimised (in a classical limit) is

$$E = \frac{C}{4} \sum_{i=1}^N (p(t) - x_i^2)^2 - \frac{1}{2} \sum_{i=1}^N \sum_{j=1}^N J_{ij} x_i x_j, \quad (1)$$

where  $x_i$  are quadratures of the OPOs,  $p(t)$  describes

the effective laser pumping power (injection minus linear losses), and  $C$  corresponds to the strength of saturable nonlinearity. As  $p(t)$  grows from a large negative to large positive  $p(t) = p_\infty$  values,  $E$  anneals from the dominant convex first term on the right-hand side of Eq. (1) that is minimized at  $x_i = 0$  for all  $i$  to the minimum of the second term which is the scaled target Ising Hamiltonian with  $x_i = \pm\sqrt{p_\infty}$ . The temporal change of  $p(t)$ , therefore, is the annealing parameter combined with a gradient descent as

$$\dot{x}_i = -\frac{\partial E}{\partial x_i} = C(p(t)x_i - x_i^3) + \sum_{i \neq j} J_{ij}x_j. \quad (2)$$

The operation of CIM, therefore, relies on the gradient descent of an annealed energy landscape. All ONN soft spin optimizers exploit this central principle, while the details of the nonlinearity or the gradient dynamics can vary from platform to platform [15]. In particular, CIM dynamics is an example of the Hopfield-Tank network (HT)  $\dot{x}_i = p(t)x_i + \sum_{i \neq j} J_{ij}x_j$  also used [26] for Ising Hamiltonian minimization [27]. Another approach uses the second-order resonance to project the XY onto the Ising dynamics [28].

Using ONNs for optimization has shown promise, yet key questions remain: ‘what are suitable benchmarks for optical machines, how to guide annealing to aid optimization, what are the ONN energy landscape dynamics during annealing to ensure the optimal state is achieved, what are the distinguishing features between quantum and classical annealing?’. Answers often rely on the coupling matrix  $\mathbf{J}$ . An instructive problem should be technologically feasible, have controllable couplings, possess non-trivial structures resistant to simple local perturbations, and be mathematically tractable. Moreover, it is better to have deterministic rather than random couplings to avoid the issues of statistical convergence [25]. We comprehensively explore ONN dynamics on circulant coupling matrices, revealing evolution patterns dictated by the eigenvalues of  $\mathbf{J}$  and the spectral gap. We identify certain unoptimizable regions using ONNs in classical annealing limits and suggest improvements via constraining soft amplitudes to their mean value.

Cyclic graphs with  $N$  nodes are characterized by an  $N \times N$  circulant coupling matrix  $\mathbf{J}$ , constructed through cyclical permutations of any  $N$ -vector. These graphs inherently have vertex permutation symmetry, signifying boundary periodicity and uniform neighbourhoods. The structure of a circulant matrix is contained in any row, and its eigenvalues and eigenvectors can be analytically derived using the  $N$  roots of unity of a polynomial, where the row components of the matrix act as coefficients:  $\lambda_n = \sum_{j=1}^N J_{1,j} \cos[\frac{2\pi n}{N}(j-1)]$  [29–31].

We consider the Ising Hamiltonian minimization on a particular form of a cyclic graph – a Möbius ladder graph with even number of vertices  $N$  such that the  $i$ ’th vertex has two edges connecting it to vertices  $i \pm 1$  with anti-

ferromagnetic coupling with strength  $J_{i,i\pm 1} = -1$  (circle couplings), and an additional antiferromagnetic coupling with vertex  $i + N/2$  with strength  $J_{i,i+N/2} = -J, J > 0$  (cross-circle couplings). We denote by  $S_0$  the state where the spins alternate along the ring so that  $s_i s_{i\pm 1} = -1$  for all  $i$  and by  $S_1$  the state where the spins alternate everywhere except at two positions on the opposite sides of the ring:  $s_i s_{i+1} = -1$  for all  $i \neq i_0$  and  $s_{i_0} s_{i_0+1} = s_{i_0+N/2} s_{i_0-1+N/2} = 1$ . When  $N/2$  is odd,  $S_0$  is always the ground state with energy  $E(J) = -(J+2)N/2$ . When  $N/2$  is even, the  $S_0$  configuration has energy  $E_0(J) = (J-2)N/2$  and  $S_1$  has energy  $E_1(J) = 4 - (J+2)N/2$ . Therefore,  $S_0$  [ $S_1$ ] is the global minimum (while  $S_1$  [ $S_0$ ] is the excited state) if  $J < J_{\text{crit}} \equiv 4/N$  [ $J_{\text{crit}} < J$ ]. The eigenvalues for Möbius ladders with  $J_{1,j} \in \{-1, 0, -J\}$  are  $\lambda_n = -2 \cos(2\pi n/N) - J(-1)^n$ . Equating the two largest eigenvalues  $2 \cos(2\pi/N) + J$  and  $2 - J$  gives the value of  $J = J_e = 1 - \cos(2\pi/N)$  at which the leading eigenvectors change. When  $J_e < J < J_{\text{crit}}$  the eigenvalues for  $S_0$  are less than that for  $S_1$  despite  $S_0$  being the lower energy state (see Supp. Inf. for the detailed derivation of the spectra).

SSIM in Eq. (1) has real amplitudes  $x_i$ . As the laser pumping  $p(t)$  increases from negative values, the minimizers  $\mathbf{x}^*$  of Eq. (1) and minima of  $E$  change. We associate Ising spins with  $x_i$  via  $s_i = x_i/|x_i|$ . We expect that the soft-spin energy state  $E_0$  that corresponds to the hard-spin Ising state  $S_0$  and depicted in Fig. (1)(a) is symmetric in amplitudes as all spins experience the same frustration of the cross-circle coupling, so all amplitudes have the same modulus  $|x_i| = X$ . From Eq. (2)  $X$  satisfies  $X = \sqrt{p(t) + (2-J)/C}$  with the corresponding soft-spin energy  $E_0 = (J-2)N(2-J+2Cp)/4$ . This state can be realised from a vacuum state when  $p(t)$  exceeds  $(J-2)/C$ .

The soft-spin energy state  $E_1$  corresponding to  $S_1$ , when two side edges are frustrated, is asymmetric in amplitudes. This asymmetry is shown schematically in Figs. (1)(b,c), in agreement with the dynamical simulations presented in Figs. (2)(b). This occurs because the lower energy is achieved if the amplitudes connected by the frustrated edges  $|x_i| = X_L$  are lower than in the rest of the system. For  $N = 8$  in Fig. (1)(b), there are two types of amplitudes: 4 nodes with  $\pm|X_L|$  and 4 with amplitudes  $|x_i| = X_B$ , where  $X_B = (1 - J - Cp)X_L + CX_L^3$  from the steady state of equation on the dynamics of  $X_L$  from Eq. (2), while the steady-state on the evolution of  $X_L$  gives  $(p+1+J)X_B + X_L = X_B^3$ . By solving the polynomial equation for  $X_L$ , we can compute  $E_1$  across any  $p, J, N$ , and  $C$ . This allows us to discern regions in this parameter space where the global minimum aligns with either  $E_0$  or  $E_1$  and confirm if these states correspond with the hard-spin Ising Hamiltonian’s global minimum. Figure (1)(d) depicts distinct regions in the  $J-p$  parameter space. Within the  $J_e < J < J_{\text{crit}}$  interval  $S_0$  emerges as the hard-spin Ising model’s lowest energy state. For the soft-spin model, however, only the

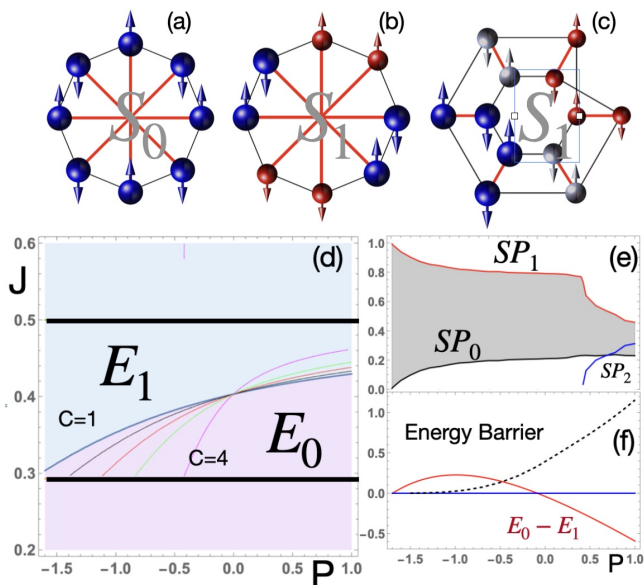


Figure 1. (a-c) Schematic representation of the states realised by soft-spin models of Eq. (1) on the Möbius ladder graphs with varying cross-ring couplings (shown in red). (a),(b) and (c) depict states that map onto  $S_0$ ,  $S_1$  Ising states for  $N = 8$  and  $S_1$  state for  $N = 12$ , respectively. (c) uses a different node arrangement that illustrates the graph relationship with the topology of the Möbius strip. The same colours are used to show equal intensities; the larger sizes correspond to larger intensities. (d) Regions of different global minima of Eq. (1):  $E_1$  in the blue region and  $E_0$  in the pink region, in  $J - p$  space for  $N = 8, C = 1$ . Two critical values of  $J$  are shown as solid black lines. Between these lines,  $S_0$  is expected as the hard-spin Ising model global minimizer. Thin lines show the contours  $E_1 = E_0$  for  $C = 1, 1.2, 1.5, 2, 4$  in that region. (e) Success probability of reaching  $E_0$  (labelled as  $SP_0$ ) and  $E_1$  (labelled as  $SP_1$ ) states of the soft-spin energy in Eq. (1) from a point  $\mathbf{x}$  with randomly chosen components  $x_i$  in  $[-1, 1]$  for different values of  $p$  and  $J = 0.4, N = 8, C = 1$ . For larger values of  $p$  a third state of higher energy appears with the success probability  $SP_2$ ; when projected on spins  $s_i = x_i/|x_i|$  this state corresponds to  $S_1$ . (f) The height of the minimum energy barrier between  $E_1$  and  $E_0$  calculated as the energy difference between  $E_1$  and energy of the nearest saddle point is shown as a black dashed line for  $J = 0.4, C = 1$ . The difference between  $E_0$  and  $E_1$  is shown in red.

region shown in pink corresponds to this state ( $E_1$ ). The bifurcation likelihood for this state is near zero, as illustrated by Fig.(1)(e). For values  $J_e < J < J_{\text{crit}}$ , as laser power  $p$  rises, the  $E_0$  state becomes the energy minimum for the soft-spin model, aligning with the hard-spin Ising Hamiltonian's  $S_0$ , shown in Fig.(1)(d). Yet, increasing amplitudes bring increased height of the energy barriers while preventing system transitions, see Fig.(1)(f). Supp. Inf. Fig.(3) provides further context, depicting attraction basins for diverse  $p$  within a fixed  $J_e < J < J_{\text{crit}}$ .

The space structure of soft spin models can be further understood by considering the critical points of their en-

ergy landscape for different annealing parameter values [32]; (see Supp. Inf). The  $S_1$  state is always further away from the origin than other critical points ( $S_0$  and saddle points). At the same time, the transition between minima  $E_0$  and  $E_1$  is possible only through a saddle point whose energy relative to  $E_1$  and  $E_0$  defines the height of the energy barriers; see Fig. (1)(f).

These considerations suggest that amplitude heterogeneities have a severely detrimental effect on the optimization process in some regions of parameter space as they allow the soft-spin energy landscape to find and follow its ground state, which is quite different from the ground state of the hard-spin Ising Hamiltonian. This problem has been recognised before [33, 34], but in the context of the final state, so various feedback schemes were suggested to bring all amplitudes to the same value, say,  $\pm 1$  at the end of the simulations. This could be achieved, for instance, by changing the laser intensity individually for each spin as  $\dot{p}_i(t) = \epsilon(1 - x_i^2)$ , where  $\epsilon$  is a small constant parameter. However, as our results on the simple circulant graphs illustrate, this feedback does not change the most essential part of the dynamics during the pitchfork bifurcation from the vacuum state. Moreover, this feedback becomes important only for amplitudes sufficiently close to  $\pm 1$  when the barriers between states are already too high.

Instead, we suggest introducing feedback restricting the soft spin energy landscape to keep them close to the average value. This restriction can be achieved by modifying the signal intensities bringing them towards the average mass per particle defined by the squared radius of the quadrature  $R(\mathbf{x}) \equiv \sum_{i=1} x_i^2/N$

$$x_i \rightarrow (1 - \delta)x_i + \delta R x_i / |x_i|. \quad (3)$$

If  $\delta = 0$ , then no adjustment is made. If  $\delta = 1$ , then all amplitudes are set to the same (average) value. For  $0 < \delta < 1$ ,  $1/\delta$  determines the proportion of the effective space for the restricted evolution.

Figure (2)e shows the probability of finding the ground state of the Ising Hamiltonian using the HT networks [26], Eq.(2) (CIM-I), Eq.(2) with individual pumping adjustments  $p \rightarrow p_i$  according to  $\dot{p}_i = \epsilon(1 - x_i^2)$  (CIM-II), and Eq.(2) with manifold reduction by Eq. (3) (CIM-III). For CIM-I and CIM-III, we set  $p(t) = (1 - p_0) \tanh(\epsilon t) + p_0$ . CIM-III shows a significant improvement in finding the ground state compared with other models. Thus, in soft-spin models, the imperative to constrain the manifold implies that dimensional annealing should be tailored according to the energy landscape's characteristics. Quantum annealing, on the other hand, harnesses dimensional annealing within an extended Hilbert space. By utilising only linear dynamics at the expense of operating within this higher-dimensional phase space, it can effectively navigate energy barriers. Next, we study the quantum evolution on the Ising energy landscape of circulant

coupling matrices in order to contrast its performance with the soft-spin nonlinear models.

We consider the transverse field Ising model with the circulant coupling matrix  $\mathbf{J}$  given by

$$\hat{H} = -\frac{1}{2} \sum_{i,j=1}^{N,N} J_{ij} \hat{S}_i^x \hat{S}_j^x - \sum_{i=1}^N h_i \hat{S}_i^z - \gamma(t) \sum_{i=1}^N \hat{S}_i^x, \quad (4)$$

$$\hat{S}_i^\alpha = \mathbf{1} \otimes \mathbf{1} \otimes \dots \otimes \mathbf{1} \otimes \hat{S}^\alpha \otimes \underbrace{\mathbf{1} \otimes \dots \otimes \mathbf{1}}_{i-1 \text{ terms}} \otimes \mathbf{1}, \quad \alpha = x, y, z, \quad (5)$$

where  $\hat{S}^\alpha$  are the spin-1/2 Pauli matrices, and  $\mathbf{1}$  is the  $2 \times 2$  identity matrix. The first term,  $\hat{H}_0$ , is diagonal and represents the classical Ising Hamiltonian  $H_I$ . We will also consider the effect of a symmetry-breaking longitudinal magnetic field given by the second term,  $\hat{H}_1$ , although initially we will exclude this term by setting  $h_i = 0$ . The transverse field,  $\hat{H}_2$ , results in a non-diagonal Hamiltonian operator and gives rise to the quantum Ising model. We set the time-dependent annealing term to  $\gamma(t) = B/\sqrt{t}$  for some constant  $B$  [35].

Our quantum system is made up of  $N$  spin-1/2 subsystems each having a basis  $|\downarrow\rangle, |\uparrow\rangle$ . A general state  $|\Psi\rangle$  of the  $N$ -spin system can then be written as  $|\Psi\rangle = \sum_{\xi} C_{\xi} |\xi\rangle$  with  $\sum_{\xi} |C_{\xi}|^2 = 1$ , where the  $C_{\xi}$ 's are complex numbers and the basis element  $|\xi\rangle \equiv |\xi_1 \dots \xi_N\rangle = |\xi_N\rangle \otimes \dots \otimes |\xi_1\rangle$ ,  $\xi_k = \{|\downarrow\rangle, |\uparrow\rangle\}$ ,  $k = 1, \dots, N$ .

We begin with an initial state that is a ground state of the Hamiltonian  $\hat{H}_2$ . The initial state at time  $t_i$  can then be expressed as  $|\Psi(t_i)\rangle = |\psi_{\rightarrow}\rangle \otimes \dots \otimes |\psi_{\rightarrow}\rangle$  where for each subsystem  $|\psi_{\rightarrow}\rangle = (|\uparrow\rangle + |\downarrow\rangle)/\sqrt{2}$ . The wavefunction is then evolved according to the time-dependent Schrödinger equation (see Supp. Inf. for details). As  $t \rightarrow \infty$ ,  $\gamma(t) \rightarrow 0$  and the contribution of  $\hat{H}_2$  decays to bring about the target Hamiltonian. Provided  $\gamma(t)$  is varied adiabatically, we can expect that the system evolves, remaining in the true ground state of the system, and settles into the target Hamiltonian's desired ground state at sufficiently long times.

To determine the probability of finding the ground state, we compute the projection of  $|\Psi(t)\rangle$  onto the ground state  $|\phi_{\text{GS}}\rangle$  of the Hamiltonian  $\hat{H}_0$  given by  $P_{\text{GS}} = |\langle \phi_{\text{GS}} | \Psi(t) \rangle|^2$ . For  $J < J_{\text{crit}}$ , the  $S_0$  ground state has a two-fold degeneracy. Therefore, we can expect that the probability of finding one of the ground states is  $P_{\text{GS}} = 1/2$ . In Fig. 2f, we present numerical simulations of the time evolution of the success probability for finding the ground state of  $N = 8$  spin system for  $J = 0.35$ . For comparison, we have also included the results for simulated annealing [36] and classical annealing by evolving a master equation [35] (see Supp. Inf. for details). In the former, we allow transition probabilities for single-spin flips only, whereas in the latter, we allow for all spin flips. As can be seen from Fig. 2f, only simulated annealing does not converge to the correct ground states of the system. In contrast, quantum and the classical annealing

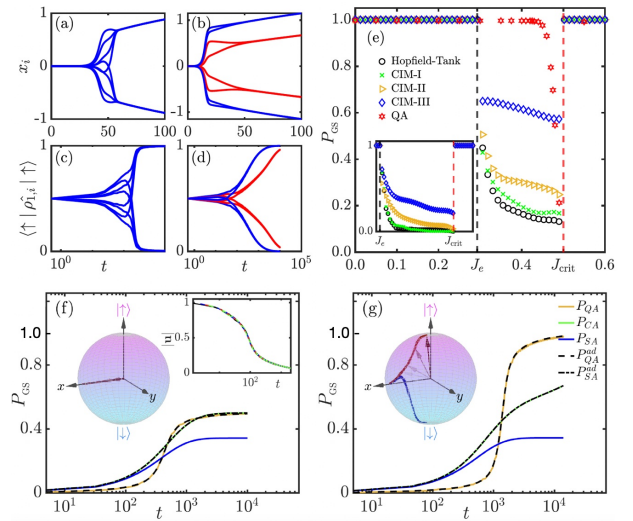


Figure 2. (a) Evolution of  $N = 8$  soft spins for  $J = 0.35$  and (b)  $J = 0.55$  according to Eq. (2). In each case, the ground state is recovered. The amplitudes connected by the frustrated edges are lower than in the rest of the system and are shown in red. In all runs,  $C = 1$ ,  $p_0 = J - 2$ ,  $\epsilon = 0.003$ ,  $\Delta t = 0.1$ , and each  $x_i(0)$  is chosen randomly from a uniform distribution in the range  $[-0.001, 0.001]$ ; (c) Similar evolution for probability amplitude of  $|\uparrow\rangle$  state in quantum annealing simulation with  $J = 0.35$  and (d)  $J = 0.6$ . The amplitudes colored in red correspond to the frustrated spins as in (b); (e) Ground state probability for HT, CIM-I, CIM-II, CIM-III, and quantum annealing (QA) for the Möbius ladder graph with  $N = 8$ . For CIM-III, for each value of  $J$  the optimum value of  $0 < \delta < 1$  is chosen based on a set of preliminary runs in which  $\delta$  is varied. Two thousand runs are used to calculate the probability of finding the ground state  $P_{\text{GS}}$  for each value of  $J$ . For QA,  $B = 5$  and  $\Delta t = 0.1$ . Inset to (e) shows the same plots but for  $N = 100$ ; (f) Ground state probability of target Hamiltonian with  $J = 0.35$  and  $B = 5$  for quantum annealing (QA), single-spin simulated annealing (SA), classical annealing (CA) and corresponding probabilities expected for adiabatic simulated (SA-ad) and adiabatic quantum (QA-ad) annealing. Insets show Bloch vector for single-spin and magnitude of Bloch vector  $|\mathbf{u}|$ ; (g) similar results as (f) but with symmetry-breaking terms added to Hamiltonian and Bloch sphere shows typical trajectories of two neighbouring spins.

recover the correct ground states even though our value of  $J$  lies within the range  $J_e < J < J_{\text{crit}}$ .

To compare the quantum annealing and semi-classical soft-spin simulations, we computed the single-spin reduced density matrix  $\hat{\rho}_{1,i}$  from the pure state  $|\Psi(t)\rangle$ . In general, the single-spin density matrix will correspond to entangled states. This is illustrated by recovering the Bloch vector from  $\hat{\rho}_{1,i}(t)$  (see Supp. Inf. for details). In the inset of Fig. (2)f, we show the evolution of the Bloch vector with time evaluated for one of the spins (other spins show similar behaviour). We see that the spin is initially aligned along the equator (consistent with the form of  $|\rightarrow\rangle$ ) but shrinks towards the origin as the state evolves. The departure of the Bloch vector from the sur-



face of the Bloch sphere is indicative of quantum entanglement while its dynamics towards the origin signals the emergence of Bell states: one of four maximally entangled states. A definite state emerges only upon measurement, which then subsequently collapses the corresponding wavefunction to one specific configuration.

For direct comparison with the deterministic semi-classical simulations, we removed the ground state degeneracy in our quantum annealing simulations by introducing the symmetry-breaking term  $\hat{H}_1$  in Eq.(4). We set  $h_i$  to correspond to  $0.05|\xi\rangle_{S_0} + 0.005|\xi\rangle_{S_1}$  where  $|\xi\rangle_{S_0}$  and  $|\xi\rangle_{S_1}$  correspond to the  $S_0$  or  $S_1$  state, respectively. This enforces the evolution towards a specific ground state without the final state being in a quantum superposition. The resulting Bloch vector for  $J = 0.35$  is shown in the inset of Fig. 2g and now indicates evolution that ends at the surface of the Bloch sphere, reaching either the  $|\uparrow\rangle$  or  $|\downarrow\rangle$  state. This evolution clearly demonstrates that though individual spins converge towards a non-correlated value, their evolution bears the imprint of inter-spin correlations. Unlike the semi-classical models, our quantum annealing algorithm consistently identifies the correct ground state in the  $J_e < J < J_{\text{crit}}$  range; (see Fig. 2e) and demonstrates that correlations play a key role in facilitating the system to converge to the true ground state. Although, its performance appears to degrade near  $J_{\text{crit}}$ , this is simply a consequence of keeping  $B$  fixed. In general  $B$  will need to be adjusted as we approach  $J_{\text{crit}}$  to account for the vanishing energy gap of the spectrum of the coupling matrix  $\mathbf{J}$ .

The corresponding time-dependent probability of finding each spin,  $i$ , in the  $|\uparrow\rangle$  state is presented in Fig. 2c for  $J = 0.35$  (and for  $J = 0.6$  in Fig. 2d). We see that even though we have strongly perturbed the system towards the  $S_1$  state for  $J = 0.35$ , the results emphasize the quantum annealing algorithm's capacity to find the correct ground state during gradual  $\gamma(t)$  quenches, leveraging the quantum system's expanded phase space.

In summary, we analysed the optimization of Ising Hamiltonians, contrasting the classical dynamics of semi-classical soft-spin models with quantum annealing. We discussed semi-classical models' challenges due to a broadening dimensionality landscape, especially when the models' global minimum maps to the Ising Hamiltonian's excited state. A solution, termed 'manifold reduction', is presented, constraining the soft-spin amplitudes and restricting the dimensionality landscape. On the other hand, we showed that quantum annealing inherently can traverse the Ising Hamiltonian's energy terrain, operating within an extensive Hilbert space. The findings highlight the importance of understanding the influence of dimensionality and the energy landscape overall on optimising physical systems. Furthermore, they demonstrate how extensions of semi-classical models to include quantum effects has the potential to assist the annealing in navigating the system towards the true ground state.

## ACKNOWLEDGEMENTS

J.S.C. acknowledges the PhD support from the EPSRC, N.G.B acknowledges the support from the Julian Schwinger Foundation Grant No. JSF-19-02-0005, HORIZON EUROPE/UKRI CL4-2021-DIGITAL-02-16, and Weizmann-UK Make Connection grant 142568.

## SUPPLEMENTARY INFORMATION

### CIRCULANT GRAPHS IN PHYSICAL SYSTEMS

An all-optical scalable ONN was recently proposed for cyclic graphs; spatial light modulators (SLMs) are used to discretize the optical field where each pixel defines a different pulse amplitude [37]. The SLM with  $M_x \times M_y$  pixels is set up with a transmission function  $\tilde{J}_k$  which multiplies the Fourier transform of the amplitudes at each round trip. The SLM couples the fields with coupling matrix  $J_{ij} \equiv \tilde{J}_{j-i+1}$ , which corresponds to a circulant graph. An alternative setup allows for any general coupling matrix. However, there is an  $N = M_x$  limit to the number of pulses. Circulant graphs such as Möbius ladders therefore lend themselves well to optical solvers, where  $N = M_x \times M_y \sim 10^6$  spins can be defined.

The couplings are often geometrical in polariton condensates, photon condensates, and laser cavities (e.g. the sign and amplitude of the coupling strength depend on the distance between condensates and outflow wavenumber [38]). The condensates arranged in a circle interact with the nearest neighbours, but the interactions beyond this decay exponentially fast. Previously, various ways of establishing long-range interactions in polariton-based XY-Ising machines were discussed. An easier way to achieve the couplings between remote sites is to use digital micro-mirror devices (DMDs) to direct the light across the ring. DMDs were shown to perform complex (amplitude and phase) modulation. By splitting the complex field into real and imaginary parts and using the time modulation scheme of the DMD, a complex signal could be synthesised [39]. Reflecting the entire ring of condensates on itself with a radial displacement implements a 3-regular cyclic graph. Cyclic graphs are known to be computationally intractable for classical computers for sampling probability distributions of quantum walks [40].

### EIGENVECTORS AND EIGENVALUES OF THE MÖBIUS LADDER COUPLING MATRIX

To find the eigenvalues and eigenvectors of  $N \times N$  matrix  $\mathbf{J}$ , for even  $n$  we use the roots of unity, so the solutions of  $\omega^N = 1$  that are  $\omega_k = \exp(i2\pi k/N)$

for  $k = 0, \dots, N-1$ . The corresponding eigenvectors are  $(1, \omega_k, \omega_k^2, \dots, \omega_k^{N-1})$  which can be verified by direct computation. Then, from the first row of  $\mathbf{J}$  we form the polynomial  $f(\omega) = -\omega - J\omega^{N/2} - \omega^{N-1}$  and evaluate it at the unit roots  $\omega_k = \exp[i2\pi k/N]$  to obtain the eigenvalues  $\lambda_k = f(\omega_k) = -2\cos(2\pi k/N) - J(-1)^k$  with the corresponding eigenvectors  $v_k = (1, \omega_k, \omega_k^2, \dots, \omega_k^{N-1})$ . The largest of  $f(\omega_k)$  is either  $\lambda_{N/2} = 2 - J$  or  $\lambda_{N/2\pm 1} = J + 2\cos(2\pi/N)$  depending on whether  $J < J_e$  or  $J > J_e$  with  $J_e \equiv 1 - \cos(2\pi/N)$  is the value where these two eigenvalues cross. The corresponding real-valued, and mutually orthogonal eigenvectors  $\mu_k$  can be formed from  $v(\omega_k)$  as  $\mu_k = \text{Re}[v(\omega_k)] + \text{Im}[v(\omega_k)]$  [30]. For two largest eigenvalues the eigenvectors are  $\mu_{N/2} = (1, -1, 1, -1, \dots, -1)$  and  $\mu_{N/2\pm 1} = (1, \pm \cos(2\pi/N) \pm \sin(2\pi/N), \dots, \pm \cos(2\pi k/N) \pm \sin(2\pi k/N), \dots, \pm \cos(2\pi(N-1)/N) \pm \sin(2\pi(N-1)/N))$ . If  $N/2$  is even, then  $\mu_{N/2\pm 1}$  have the components with two zero values at the positions separated by  $N/2 - 1$  sign alternating components.

We illustrate this construction for the Möbius ladder coupling matrix  $\mathbf{J}$  with  $N = 8$  considered in the main text

$$\mathbf{J} = \begin{pmatrix} 0 & -1 & 0 & 0 & -J & 0 & 0 & -1 \\ -1 & 0 & -1 & 0 & 0 & -J & 0 & 0 \\ 0 & -1 & 0 & -1 & 0 & 0 & -J & 0 \\ 0 & 0 & -1 & 0 & -1 & 0 & 0 & -J \\ -J & 0 & 0 & -1 & 0 & -1 & 0 & 0 \\ 0 & -J & 0 & 0 & -1 & 0 & -1 & 0 \\ 0 & 0 & -J & 0 & 0 & -1 & 0 & -1 \\ -1 & 0 & 0 & -J & 0 & 0 & -1 & 0 \end{pmatrix}. \quad (6)$$

The eigenvalues are  $\lambda_0 = f(\omega_0) = f(1) = -2 - J$ ,  $\lambda_1 = f(\omega_1) = -\sqrt{2} + J$ ,  $\lambda_2 = f(\omega_2) = -J$ ,  $\lambda_3 = f(\omega_3) = \sqrt{2} + J$ ,  $\lambda_4 = f(\omega_4) = 2 - J$ ,  $\lambda_5 = f(\omega_5) = \sqrt{2} + J$ ,  $\lambda_6 = f(\omega_6) = -J$ , and  $\lambda_7 = f(\omega_7) = -\sqrt{2} + J$ .

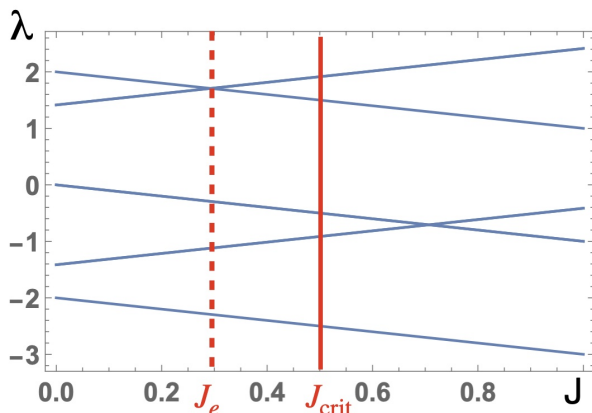


Figure 3. Eigenvalues of the Möbius ladder graph for  $N = 8$  as functions of  $J$ .  $J_e$  is the value of  $J$  where the red dashed line shows the two largest eigenvalues cross.  $J_{\text{crit}}$  shows where their energies equal  $E_1 = E_0$ . The ground state corresponds to  $S_0$  for  $J < J_{\text{crit}}$  and  $S_1$  for  $J > J_{\text{crit}}$ .

The eigenvector that corresponds to  $\lambda_3$  is  $\mu_3 = (1, -1, 1, -1, 1, -1, 1, -1)$  and the eigenvector that corresponds to, say,  $\lambda_4$  is  $\mu_4 = (1, -\sqrt{2}, 1, 0, -1, \sqrt{2}, -1, 0)$ . The soft spin system, therefore, follows  $(+, -, +, +, -, +, -, -)$  or  $(+, -, +, -, -, +, -, +)$  direction at the onset of the pitchfork bifurcation when  $J > J_e$  while  $\lambda_4$  becomes the dominant eigenvalue of matrix  $\mathbf{J}$ . Figure 3 illustrates how these eigenvalues vary as a function of  $J$ .

## BASINS OF ATTRACTION

Figure 4 depicts the basins of attraction for various  $p$  and fixed  $J_e < J < J_{\text{crit}}$ . The basins of attraction are defined as the sets of points randomly distributed on  $[-1, 1]$  from which the gradient descent leads to different minima. At the threshold of large negative  $p$ , the basin of attraction of  $E_1$  (which is the ground state of  $E$  as given by Eq. (1) of main text) dominates. As  $p$  increases, the basin of attraction of the excited state  $E_0$  increases while at small positive values of  $p$ ,  $E_0$  becomes the ground state. With a further increase of  $p$  other states with even higher energy appear.

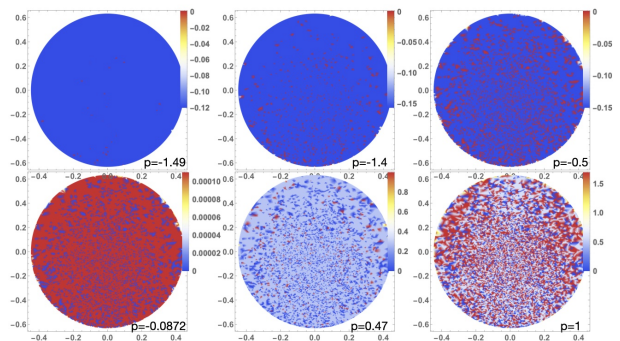


Figure 4. Basins of attraction of the soft spin energy in Eq. (2) as defined in the main text. We take  $N = 8$ ,  $J = 0.4$ ,  $C = 1$ , various laser powers  $p$ , 20,000 randomly distributed  $x_i$  in  $[-1, 1]$  and show which minimum is reached via gradient descent using Newton's method. To characterise points, the average magnetization  $m = \sum_i x_i/N$  (vertical axis) and the correlations along the circle between  $x_i$  defined as  $X_{\text{corr}} = \sum_i (x_i - m)(x_{i+1} - m) / \sum_i (x_i - m)^2$  (horizontal axis), are used. For small  $p$ , the basin of attraction is dominated by  $S_1$  state as any initial state descends to  $E_1$ . As  $p$  grows, the ratio of the volume of the basins of attraction of the  $S_1$  state to the volume of the basins of attraction of the  $S_0$  approaches 4. At the critical value of  $p \approx -0.08715$ , both  $S_1$  and  $S_0$  states have the same energy, and after that  $S_0$  state becomes the ground state: this is indicated by the switch between ground (blue) and excited (red) states.

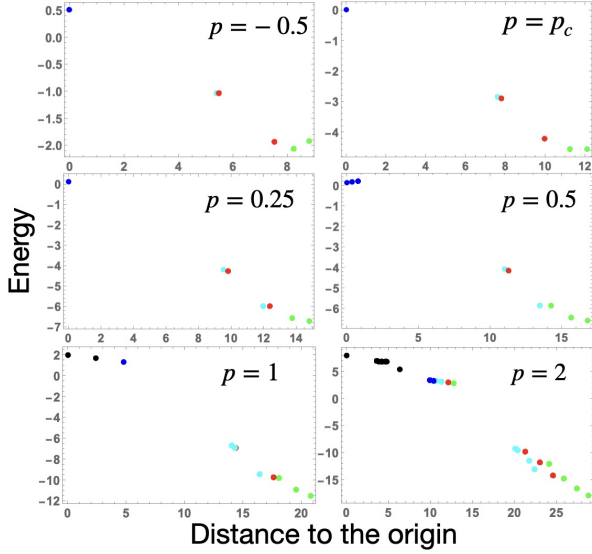


Figure 5. Critical points of the CIM energy (defined by Eq. (1) of the main text) for  $N = 8, C = 1$  and different values of laser power  $p$ . Minima are shown in green, saddles with one, two, three and 4+ unstable directions are shown as red, light blue, blue and black points, respectively. The  $S_0$  state is furthest from the origin, which becomes the global minimum for  $p > p_c = -0.0872$ . The minima for  $p = 2$  are  $S_0, S_1, (-, -, +, -, +, -, -, +), (+, -, -, +, +, -, +, -)$  and  $(+, -, -, +, +, -, -, +)$  in increasing energy.

### CRITICAL POINTS

The main text gives the energy of the CIM  $E$  in Eq. (1). We can determine the critical (minima and the saddle) points by setting  $\partial E / \partial x_i = 0$  for all  $i = 1, \dots, N$  and classify them using the Hessian matrix. The number of critical points grows exponentially fast with  $p$ ; however, not in terms of energy and the distance from the state  $x_i = 0 \forall i$  as Fig. 5 illustrates.

### SOLUTION OF THE TIME-DEPENDENT SCHRÖDINGER EQUATION

The wavefunction is evolved according to the time-dependent Schrödinger equation (with  $\hbar = 1$ ) given by

$$i \frac{d}{dt} |\Psi(t)\rangle = \hat{H}(t) |\Psi(t)\rangle, \quad (7)$$

$$\hat{H}(t_i) |\Psi(t_i)\rangle = \epsilon_{gs} |\Psi(t_i)\rangle, \quad (8)$$

where  $\epsilon_{gs}$  denotes the ground state energy of the system at the initial time.

To evolve the time-dependent Hamiltonian given by Eq.(7), we use a second order accurate Strang time-splitting method where  $\hat{H}_0$  is evolved for half a time-step  $\Delta t$  followed by  $\hat{H}_1$  for a full time-step and then  $\hat{H}_0$  for another half a time-step. The resulting time-integration

scheme can then be written as

$$|\Psi(t_{n+1})\rangle = \exp\left(-i \frac{\Delta t}{2} \hat{H}_D\right) \left(-\frac{i}{2} \int_{t_n}^{t_{n+1}} \hat{H}_2(\tilde{t}) d\tilde{t}\right) \times \exp\left(-i \frac{\Delta t}{2} \hat{H}_D\right) |\Psi(t_n)\rangle, \quad (9)$$

where  $\hat{H}_D = \hat{H}_0 + \hat{H}_1$  is the diagonal part of the Hamiltonian operator.

By placing the Hamiltonian operator  $\hat{H}_2(t)$  containing the time-dependent term in the middle of the split-step algorithm, we ensure that we have a symmetric time-splitting method. The time integral appearing in Eq. (9) was evaluated analytically. In our simulations, we set  $\Delta t \equiv t_{n+1} - t_n = 0.1$ . The simulations were performed in MATLAB. The exponentials of the diagonal and non-diagonal Hamiltonian can then be readily evaluated using the `expm` function [41].

### COMPUTATION OF BLOCH VECTORS IN QUANTUM ANNEALING SIMULATIONS

The single-spin reduced density matrix  $\hat{\rho}_{1,k}$  is obtained by taking the partial trace of the  $2^N \times 2^N$  density matrix  $\hat{\rho}$  over the Hilbert space of the other  $N - 1$  spins. For the  $k$ 'th spin, this is defined as

$$\hat{\rho}_{1,k}(t) = \text{Tr}_{\{N \setminus k\}} \hat{\rho}, \quad (10)$$

where  $\{N \setminus k\}$  denotes the  $N$  spin Hilbert space excluding the  $k$ 'th spin. The single-spin density matrix can then be parameterised as

$$\hat{\rho}_{1,k} = \frac{1}{2} (\mathbb{1} + \mathbf{u}_k \cdot \hat{\mathbf{S}}) = \frac{1}{2} \begin{pmatrix} 1 + w_k & u_k - i v_k \\ u_k + i v_k & 1 - w_k \end{pmatrix}, \quad (11)$$

where  $\mathbf{u}_k = (u_k, v_k, w_k)$  defines the corresponding Bloch vector and  $\hat{\mathbf{S}} = (\hat{S}^x, \hat{S}^y, \hat{S}^z)$  correspond to the vector of spin-1/2 Pauli matrices. For pure states the single-spin reduced density matrix has rank 1, with a magnitude of the Bloch vector  $|\mathbf{u}_k| = 1$ . The surface of the Bloch sphere, therefore, represents all the possible pure states whereas the interior of the sphere corresponds to mixed states. The collapse of the Bloch vector towards the origin implies that the state represents a maximally entangled Bell-like state.

### MASTER EQUATION FOR CLASSICAL/SIMULATED ANNEALING

To model simulated annealing, we follow the method described in [35] and introduce the Master equation for the transition probability  $P_i(t)$  for each spin configuration.

$$\frac{dP_i(t)}{dt} = \sum_{j=1}^{2^N} A_{ij}(t) P_j(t) \quad (12)$$

The  $2^N \times 2^N$  matrix  $A_{ij}(t)$  describes the transition rates. The master equation can be written in the form

$$\frac{dP_i(t)}{dt} = \sum_{i \neq j} A_{ij}(t)P_j(t) + A_{ii}(t)P_i(t) \quad (13)$$

$$= \sum_{i \neq j} (A_{ij}(t)P_j(t) - A_{ji}(t)P_i(t)) \quad (14)$$

where we have made use of the conservation of probability given by

$$\frac{d}{dt} \sum_j P_j(t) = \sum_{i,j} (A_{ji}P_i) = 0, \quad (15)$$

to arrive at the final equality. Since the normalisation condition must hold for any probabilities  $P_j$ , it follows that

$$\sum_j A_{ji} = 0, \quad \text{or} \quad A_{ii} = - \sum_{i \neq j} A_{ji}. \quad (16)$$

Using Eq.(16) to represent the diagonal terms of the Master equation ensures that a numerical integration of this equation continues to conserve the normalisation of the probabilities.

The precise form of the transition probabilities is problem specific although it is common to use the Boltzmann distribution. In our work, we follow [35] and use the Bose-Einstein distribution such that

$$A_{ij}(t) = \begin{cases} \left\{ 1 + \exp \left[ \frac{(E_i - E_j)}{T(t)} \right] \right\}^{-1}, & (\text{single-spin flip}) \\ - \sum_{k \neq i} A_{ki}, & (i = j) \\ 0, & (\text{otherwise}). \end{cases}$$

The form given above that is used for our simulated annealing simulations means that entries of  $A_{ij}$  are non-zero only for transitions corresponding to single-spin flips. The annealing is performed by varying the temperature  $T(t)$  with time. To maintain consistency with our quantum annealing simulations, we have varied the temperature according to  $T(t) = D/\sqrt{t}$ , where  $D$  is a free parameter which we set to  $D = 5$ .

For our classical annealing (CA) simulations, we did not zero out any of the transition probabilities in order to infer how collective transitions of spins at each time-step, as opposed to only single-spin transitions, affects the performance of classical algorithms. Such collective transitions can be important when topological constraints associated with particular spin configurations can render certain single-spin transitions ineffective at escaping local energy minima. It is also useful to make the observation that quantum and classical annealing can be closely related to one another if one formulates quantum annealing in imaginary time following a Wick rotation. It then follows that the evolution of the  $N$ -spin wavefunction  $|\Psi(t)\rangle$  is given by

$$\frac{d}{dt} |\Psi(t)\rangle = (\mu(t) - \hat{H}(t)) |\Psi(t)\rangle. \quad (17)$$

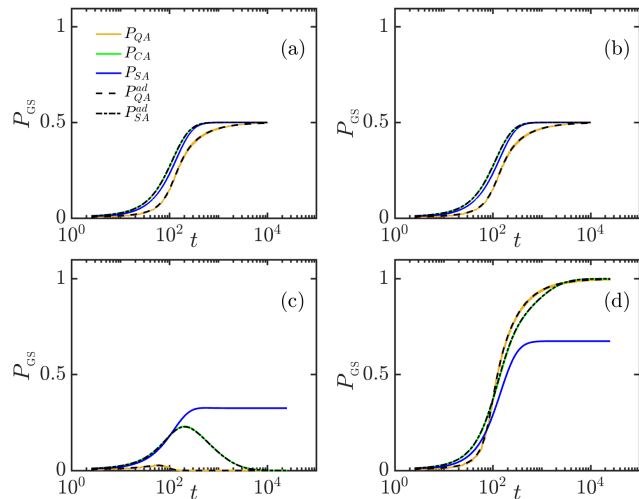


Figure 6. Time-evolution of ground state probability of target Hamiltonian with  $J = 0$  and  $B = 5$  for quantum annealing (QA), single-spin simulated annealing (SA), classical annealing (CA) and corresponding probabilities expected for adiabatic simulated (SA-ad) and adiabatic quantum (QA-ad) annealing. (a) and (b) correspond to simulation without symmetry breaking term which corresponds to a doubly degenerate ground state. Each figure corresponds to the projection of the probability density onto each one of the ground states; (c) and (d) correspond to a simulation with a symmetry breaking term added which lifts the degeneracy and leads to a unique ground state.

Here,  $\mu(t)$  plays the role of a Lagrange multiplier which ensures that the normalisation of the wavefunction is conserved in analogy with the modification introduced above to the diagonal term of the Master equation. Therefore, by comparing quantum annealing, simulated annealing, and classical annealing, we can distinguish between the effects of retaining all-spin transitions from the difference of evolving our equations in real and imaginary time.

## RESULTS OF QUANTUM ANNEALING SIMULATIONS

Here, we include additional simulation results to complement the results presented in the main text. In Figs. 2f and 2g of the main text, we presented results for the time evolution of the ground state probability for  $J = 0.35$  and  $B = 5$ . In Fig. 4, we also present results for  $J = 0$  for the probability amplitude of the eigenstates with the two energy minima to discern the role of groundstate degeneracy and how this is lifted by the symmetry breaking terms. In Figs. 6a and 6b we present simulations for the case where no symmetry breaking term is included so that the system contains two degenerate energy minima. Time evolution of the probabilities for finding the system in one of the two degenerate ground states show an



equal probability for the system to be found in either one of these states. Moreover, the results are relatively similar regardless of which numerical method is considered. Therefore, all models including quantum annealing, simulated annealing and classical annealing show a similar performance in tracking the ground states as indicated by the curves representing adiabatic evolution of the system.

In Figs. 6c and 6d we present simulations for the case where a symmetry breaking term is included as in the main text. Here, we used  $0.05|\xi\rangle_{S_0} + 0.05|\xi\rangle_{S_1}$  to introduce the symmetry breaking term. In contrast to the previous case, the behaviour of the different models is now markedly different. In particular, we observe that both quantum annealing and classical annealing correctly evolve with the true ground state as indicated by the curves corresponding to the adiabatic evolution. Moreover, due to the symmetry breaking there is one unique ground state that the two methods can follow. In contrast, simulated annealing is not always successful at tracking the true ground state even for this case where  $J = 0$ . We found a success probability of only 67%, whereas the remaining probability is associated with the system converging to what is now a metastable state.

These results demonstrate the importance of the symmetry breaking terms and how they affect the time-evolution of the ground state probabilities. In order to perform a more systematic study of the impact of including the symmetry breaking terms, in Fig. 7 we present results for simulations performed by using a symmetry breaking term of the form  $0.05|\xi\rangle_{S_0} + h_1|\xi\rangle_{S_1}$ , where  $h_1$  is varied from 0.005 to 0.1. For each value of  $h_1$ , we have evaluated the time evolution of the probability amplitudes  $\langle \uparrow | \hat{\rho}_{1,k} | \uparrow \rangle$  for each spin  $k$  as well as the time evolution of the magnitude of the corresponding Bloch vectors  $|\mathbf{u}_k|$ . The results demonstrate that as  $h_1$  is increased, the initial evolution of the probability amplitudes is to align the spins towards the  $S_1$  state which is caused by the increasing contribution of the symmetry breaking term. However, as the system navigates the energy landscape, quantum correlations develop as indicated by the decreasing amplitude of the Bloch vectors of the individual spins. This emerging quantum entanglement of the spins prevents the system from becoming stuck in local energy minima and subsequently allows the spins to readjust in order to track the true ground state. Subsequently the system converges to the true ground state that is well described by a pure state as the magnitude of the Bloch vectors converge to unity. We note that during the evolution, the maximal entanglement occurs at the time when the projection of some of the spins flips to the opposite direction. This time also coincides with the time where simulated annealing fails to track the correct ground state in comparison to quantum annealing as reflected in the results of Figs. 6c and 6d. We, therefore, conclude that quantum correlations play a key role in

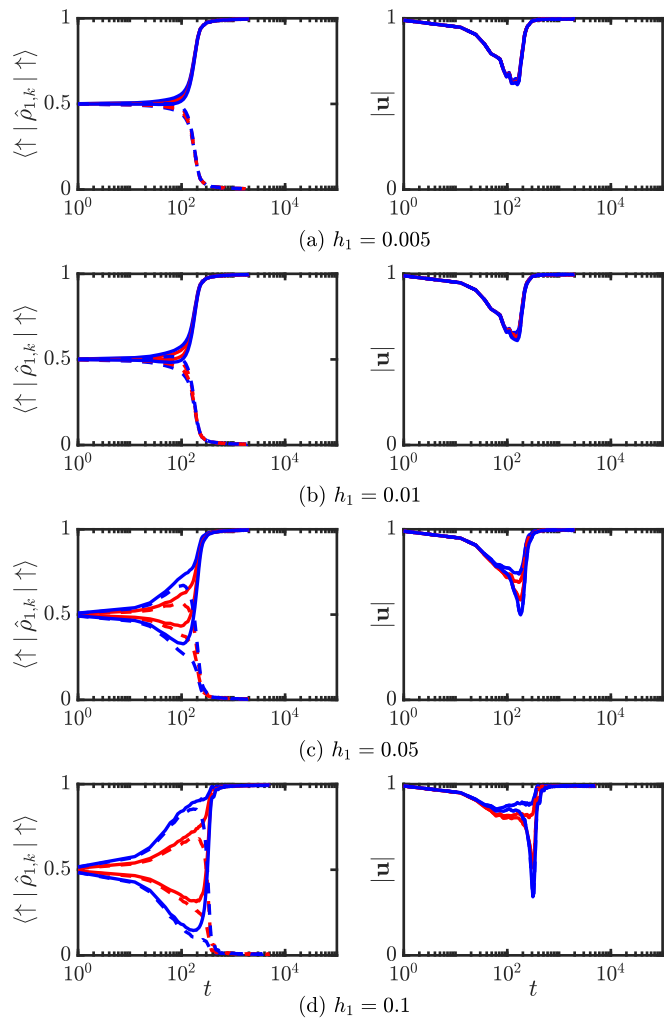


Figure 7. Time-evolution of probability amplitude of  $|\uparrow\rangle$  state (left panels) and magnitude of Bloch vectors (right panels) in quantum annealing computation with  $J = 0.35$  and  $B = 5$ . The dashed lines correspond to spins that at the end of the annealing align along the  $|\downarrow\rangle$  state whereas solid lines correspond to spins that align with the  $|\uparrow\rangle$  state. The red and blue colored lines correspond to the color of the spins shown in Fig. 1b of main text.

allowing quantum annealing to outperform other methods in this region of the parameter space of the Möbius circulant graph.

\* correspondence address: [N.G.Berloff@damtp.cam.ac.uk](mailto:N.G.Berloff@damtp.cam.ac.uk)

- [1] J. Kasprzak, M. Richard, S. Kundermann, A. Baas, P. Jeambrun, J. Keeling, F. Marchetti, M. Szymańska, R. André, J. Staehli, et al., *Nature* **443**, 409 (2006).
- [2] Y. Yamamoto, K. Aihara, T. Leleu, K.-i. Kawarabayashi, S. Kako, M. Fejer, K. Inoue, and H. Takesue, *npj Quantum Information* **3**, 1 (2017).
- [3] T. Inagaki, Y. Haribara, K. Igarashi, T. Sonobe, S. Tamate, T. Honjo, A. Marandi, P. L. McMahon, T. Umeki,

- K. Enbutsu, et al., *Science* **354**, 603 (2016).
- [4] P. L. McMahon, A. Marandi, Y. Haribara, R. Hamerly, C. Langrock, S. Tamate, T. Inagaki, H. Takesue, S. Utsunomiya, K. Aihara, et al., *Science* **354**, 614 (2016).
- [5] T. Honjo, T. Sonobe, K. Inaba, T. Inagaki, T. Ikuta, Y. Yamada, T. Kazama, K. Enbutsu, T. Umeki, R. Kasahara, K. ichi Kawarabayashi, and H. Takesue, *Science Advances* **7**, eabh0952 (2021), <https://www.science.org/doi/pdf/10.1126/sciadv.abh0952>.
- [6] V. Pal, S. Mahler, C. Tradonsky, A. A. Friesem, and N. Davidson, *Physical Review Research* **2**, 033008 (2020).
- [7] M. Babaeian, D. T. Nguyen, V. Demir, M. Akbulut, P.-A. Blanche, Y. Kaneda, S. Guha, M. A. Neifeld, and N. Peyghambarian, *Nature communications* **10**, 1 (2019).
- [8] M. Parto, W. Hayenga, A. Marandi, D. N. Christodoulides, and M. Khajavikhan, *Nature materials* **19**, 725 (2020).
- [9] D. Pierangeli, G. Marcucci, and C. Conti, *Physical review letters* **122**, 213902 (2019).
- [10] N. G. Berloff, M. Silva, K. Kalinin, A. Askitopoulos, J. D. Töpfer, P. Cilibrizzi, W. Langbein, and P. G. Lagoudakis, *Nature materials* (2017).
- [11] K. P. Kalinin, A. Amo, J. Bloch, and N. G. Berloff, *Nanophotonics* **9**, 4127 (2020).
- [12] M. Vretenar, B. Kassenberg, S. Bissesar, C. Toebes, and J. Klaers, *Physical Review Research* **3**, 023167 (2021).
- [13] K. Kalinin, G. Mourgias-Alexandris, H. Ballani, N. G. Berloff, J. H. Clegg, D. Cletheroe, C. Gkantsidis, I. Haller, V. Lyutsarev, F. Parmigiani, L. Pickup, et al., *arXiv preprint arXiv:2304.12594* (2023).
- [14] H. Goto, K. Endo, M. Suzuki, Y. Sakai, T. Kanao, Y. Hamakawa, R. Hidaka, M. Yamasaki, and K. Tatumura, *Science Advances* **7**, eabe7953 (2021).
- [15] M. Syed and N. G. Berloff, “Physics-enhanced bifurcation optimisers: All you need is a canonical complex network,” (2022).
- [16] M. Calvanese Strinati and C. Conti, *Nature Communications* **13**, 7248 (2022).
- [17] C.-W. Liu, A. Polkovnikov, and A. W. Sandvik, *Phys. Rev. Lett.* **114**, 147203 (2015).
- [18] A. D. King, S. Suzuki, J. Raymond, A. Zucca, T. Lanting, F. Altomare, A. J. Berkley, S. Ejtemaee, E. Hoskinson, S. Huang, E. Ladizinsky, A. J. R. MacDonald, G. Marsden, T. Oh, G. Poulin-Lamarre, M. Reis, C. Rich, Y. Sato, J. D. Whittaker, J. Yao, R. Harris, D. A. Lidar, H. Nishimori, and M. H. Amin, *Nature Physics* **18**, 1324 (2022).
- [19] B. Heim, T. F. Rønnow, S. V. Isakov, and M. Troyer, *Science* **348**, 215 (2015), <https://www.science.org/doi/pdf/10.1126/science.aaa4170>.
- [20] A. D. King, J. Raymond, T. Lanting, R. Harris, A. Zucca, F. Altomare, A. J. Berkley, K. Boothby, S. Ejtemaee, C. Enderud, E. Hoskinson, S. Huang, E. Ladizinsky, A. J. R. MacDonald, G. Marsden, R. Molavi, T. Oh, G. Poulin-Lamarre, M. Reis, C. Rich, Y. Sato, N. Tsai, M. Volkmann, J. D. Whittaker, J. Yao, A. W. Sandvik, and M. H. Amin, *Nature* **617**, 61 (2023).
- [21] T. Albash and D. A. Lidar, *Phys. Rev. X* **8**, 031016 (2018).
- [22] B. Yan and N. A. Sinitsyn, *Nature Communications* **13**, 2212 (2022).
- [23] T. Albash and D. A. Lidar, *Phys. Rev. X* **8**, 031016 (2018).
- [24] R. Hamerly, T. Inagaki, P. L. McMahon, D. Venturelli, A. Marandi, T. Onodera, E. Ng, C. Langrock, K. Inaba, T. Honjo, K. Enbutsu, T. Umeki, R. Kasahara, S. Utsunomiya, S. Kako, K. ichi Kawarabayashi, R. L. Byer, M. M. Fejer, H. Mabuchi, D. Englund, E. Rieffel, H. Takesue, and Y. Yamamoto, *Science Advances* **5**, eaau0823 (2019), <https://www.science.org/doi/pdf/10.1126/sciadv.aau0823>.
- [25] B. P. Marsh, R. M. Kroeze, S. Ganguli, S. Gopalakrishnan, J. Keeling, and B. L. Lev, “Entanglement and replica symmetry breaking in a driven-dissipative quantum spin glass,” (2023), [arXiv:2307.10176 \[quant-ph\]](https://arxiv.org/abs/2307.10176).
- [26] J. J. Hopfield, *Proceedings of the national academy of sciences* **79**, 2554 (1982).
- [27] J. J. Hopfield and D. W. Tank, *Biological cybernetics* **52**, 141 (1985).
- [28] K. P. Kalinin and N. G. Berloff, *arXiv preprint arXiv:1806.11457* (2018).
- [29] D. Kalman and J. E. White, *The American Mathematical Monthly* **108**, 821 (2001).
- [30] H. Zhang and Y. Yang, *International journal of quantum chemistry* **107**, 330 (2007).
- [31] J. Gancio and N. Rubido, *Chaos, Solitons & Fractals* **158**, 112001 (2022).
- [32] A. Yamamura, H. Mabuchi, and S. Ganguli, “Geometric landscape annealing as an optimization principle underlying the coherent ising machine,” (2023), [arXiv:2309.08119 \[cond-mat.dis-nn\]](https://arxiv.org/abs/2309.08119).
- [33] K. P. Kalinin and N. G. Berloff, *New Journal of Physics* **20**, 113023 (2018).
- [34] T. Leleu, F. Khoystatee, T. Levi, R. Hamerly, T. Kohno, and K. Aihara, *arXiv e-prints*, *arXiv* (2020).
- [35] T. Kadowaki and H. Nishimori, *Phys. Rev. E* **58**, 5355 (1998).
- [36] S. Kirkpatrick, C. D. Gelatt, and M. P. Vecchi, *Science* **220**, 671 (1983), <https://www.science.org/doi/pdf/10.1126/science.220.4598.671>.
- [37] M. Calvanese Strinati, D. Pierangeli, and C. Conti, *Phys. Rev. Appl.* **16**, 054022 (2021).
- [38] H. Ohadi, R. Gregory, T. Freearde, Y. Rubo, A. Kavokin, N. Berloff, and P. Lagoudakis, *Physical Review X* **6**, 031032 (2016).
- [39] A. B. Ayoub and D. Psaltis, *Scientific Reports* **11**, 1 (2021).
- [40] X. Qiang, T. Loke, A. Montanaro, K. Aungkunsiri, X. Zhou, J. L. O’Brien, J. B. Wang, and J. C. Matthews, *Nature communications* **7**, 1 (2016).
- [41] A. Norambuena, D. Tancara, and R. Coto, *European Journal of Physics* **41**, 045404 (2020).